# A Ladder-type Heteroheptacene 12H-Dithieno[2′,3′:4,5]thieno[3,2-b:2′,3′-h]fluorene Based D-A Copolymer with Strong Intermolecular Interactions toward Efficient Polymer Solar Cells

Mingyan Yang,[†] Tsz-Ki Lau,[‡] Shengqiang Xiao,*,[†] Jianhong Gao,[†] Wei Wang,[†] Xinhui Lu,*,[‡] Shoujie Zhang,[†] Jiansheng Wu,[†] Chun Zhan,[†] and Wei You*,[†,§]

[†]State Key Laboratory of Advanced Technology for Materials Synthesis and Processing, Wuhan University of Technology, Wuhan 430070, P. R. China

[‡]Department of Physics, Chinese University of Hong Kong, Hong Kong, P. R. China

[§]Department of Chemistry, University of North Carolina at Chapel Hill, Chapel Hill, North Carolina 27599-3290, United States

**ABSTRACT:** Ladder-type electron-donating units for D-A copolymers applied in polymer solar cells usually comprise multiple tetrahedral carbon bridges bonded with out-of-plane alkyl chains for desirable solubility for device processing. However, molecular packing of resultant copolymers in the solid state and charge transport within devices are also impeded in spite of with multiple fused aromatic backbones. To mitigate this issue, a structurally well-defined ladder-type electron-donating heteroheptacene, 12H-dithieno[2′,3′:4,5]thieno[3,2-b:2′,3′-h]fluorene (**DTTF**) with an extended conjugated backbone and a single tetrahedral carbon bridge attached with two bulky alkyl chains was designed and synthesized. The copolymerization of **DTTF** with 4,7-bis(4-hexylthiophen-2-yl)benzo[c][1,2,5]thiadiazole (**DTBT**) afforded a soluble D-A copolymer (**PDTTF-DTBT**) with a medium optical band gap of 1.72 eV and low-lying HOMO level at −5.36 eV. **PDTTF-DTBT** unprecedentedly exhibits strong intermolecular stacking ability and presents preferential face-on orientation on both ZnO and PEDOT:PSS layers. The improved packing order and appropriate phase separation of both the copolymer and PC$_{71}$BM in the bulk heterojunction blend on the ZnO layer over on the PEDOT:PSS layer lead to much improved power conversion efficiency of ∼8.2% in the inverted solar cell device, among the highest for reported ladder-type D-A copolymers. The research demonstrates that it is an effective method to incorporate a single tetrahedral carbon bridge to the molecular center of a ladder-type heteroacene with heavily extended π-conjugation to prepare D-A copolymers toward highly efficient PSCs.

**KEYWORDS:** heteroheptacenes, ladder-type conjugated polymers, polymer solar cells, bulk heterojunction, morphology, device configuration
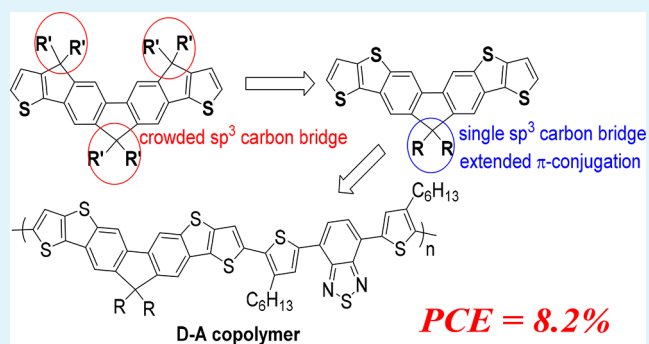
## 1. INTRODUCTION

Bulk heterojunction (BHJ) polymer solar cells (PSCs), typically consisting of an active layer with a mixture of a p-type polymer and an n-type organic semiconductor, have attracted extensive attention in recent years. Significant progress has been made in the past decades, with the maximum power conversion efficiency (PCE) of a polymer:fullerene BHJ blend already approaching 12% for single-junction devices.[1−6] This encouraging result was primarily enabled by the continuous efforts on the design and synthesis of novel conjugated polymers as well as on morphology control, interface modification, and device engineering.[7−13] Very recently, PCE values of PSCs were even pushed forward to 13% by using emerged ladder-type non-fullerene electron acceptors with dicyanomethylene indanone

subunits.[14−17] Developing novel highly efficient p-type polymers further will definitely keep enhancing the prospective of PSCs to become a real renewable energy conversion technology. In general, the molecular structure of a p-type conjugated polymer should be carefully designed by focusing on the correlations of its optical and electronic properties (in particular, in the solid state) with the characteristics of its BHJ device, including short-circuit current ($J_{sc}$), open-circuit voltage ($V_{oc}$), and fill factor (FF). In addition, the morphology (broadly defined, including molecular packing/stacking and nanoscale

phase separation information) of such BHJ blend also plays a very important role. This is because conjugated polymers having the "ideal" energy levels and band gaps could end up with poor device performance if the morphology of BHJ blends were not optimal.[18]

Ideally, a p-type conjugated polymer for highly efficient PSCs should have desirable properties as the following: sufficient solubility to guarantee solution processability, a suitable downhill energy offset with the pairing n-type materials for efficient exciton dissociation, a low highest occupied molecular orbital (HOMO) level to attain a high $V_{oc}$, an effective band gap ($E_g$) to achieve a high $J_{sc}$, and a high hole mobility as well as optimized molecular orientation in the solid state to promote effective charge transport for achieving a high FF. One of the most effective approaches to construct such an "ideal" polymer is to synthesize a donor−acceptor (D-A) copolymer with alternating D and A structural units. Numerous conjugated polymers have been successfully brought forth by this approach with exceptional photovoltaic device performance because of the high flexibility in tuning the energy levels and band gaps of the resultant D-A copolymers.[19] Within the D-A copolymers, electron-donating structural units (i.e., D) have received much more attention than the electron-deficient structural units (i.e., A). Heteroacenes, particularly with thiophenes installed at both ends of the acenes such as tricyclic benzodithiophene (BnDT), are the most successful building blocks for donor units and allow one to finely tune the HOMO level and to achieve a broad absorption of resulting D-A copolymers.[20−23] In addition, the coplanarity introduced by these structurally rigid heteroacenes can facilitate the desirable molecular assembly in solid state through intermolecular interactions and additional sulfur−sulfur (S−S) interactions. However, such rigid conjugated backbones often lead to significantly decreased solubility in processing solvents. Thus, one would have to add long alkyl side chains to these heteroacenes for desirable solubility. This strategy involves significant efforts in synthesis.[24,25] To mitigate this solubility/processability issue, ladder-type structures have been developed to contain multiple fused heterocyclic aromatics with more flexible alkyl side chains. In practice, many ladder-type electron-donating structural units have been utilized in the preparation of p-type D-A copolymers with the maximum PCE close to 8% achieved.[26−28] Most of such ladder-type heterocyclic aromatics introduced multiple sp³-hybridized carbon bridges between adjacent conjugated units to overcome the solubility issue of resultant D-A copolymers. Unfortunately, the out-of-plane arrangement of dense alkyl side chains on such multiple tetrahedral bridges would negatively impact the desirable molecular assembly in the solid state.[26,29]

In order to enjoy the benefits of increased solubility by these alkyl chains on sp³-hybridized carbon bridges yet largely retaining the molecular assembly in the solid state, we envisioned that introducing a single sp³-hybridized carbon bridge into the center of a heteroacene, where two bulky alkyl chains could be attached to the bridge, would achieve the solubility of such D-A conjugated polymers as well. Further, we hypothesized that adding more fused aromatics to the heteroacene on both ends to extend the π-conjugation would help to retain the molecular assembly (e.g., packing) in the solid state. Chart 1 presents the design rationale with one such example, 12H-dithieno[2′,3′:4,5]thieno[3,2-b:2′,3′-h]fluorene (DTTF). In this newly designed structural unit, the presence of a fluorene unit in the center offers a single sp³-hybridized

12H-dithieno[2′,3′:4,5]thieno[3,2-b:2′,3′-h]fluorene (DTTF)



**PDTTF-DTBT**     R = 2-hexyldecyl
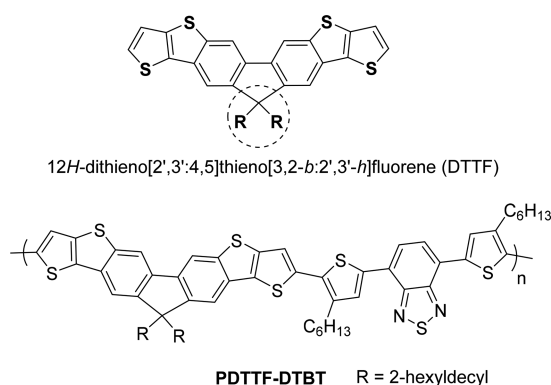
carbon bridge with two attached bulky side chains, and the thienothiophenes fused at both ends of the fluorene unit would extend the conjugation to allow the intermolecular interaction among polymers for the desirable molecular assembly.

In this contribution, we report the synthesis of the novel ladder-type heteroheptacene building block of DTTF and its application as a donor unit to make a D-A copolymer for highly efficient PSCs. DTTF can be readily obtained after six synthetic steps starting from 3,6-dibromofluorene. The copolymerization of DTTF with a common acceptor unit of 4,7-bis(4′-hexylthiophen-2-yl)benzo[c][1,2,5]thiadiazole (DTBT) affords a novel soluble D-A copolymer PDTTF-DTBT (Chart 1) with a medium optical band gap of 1.72 eV and a low-lying HOMO level at −5.36 eV. PDTTF-DTBT indeed exhibits a strong intermolecular stacking ability and presents a preferential face-on orientation in film on both ZnO layer (in the inverted device architecture) and PEDOT:PSS layer (in the conventional device architecture). Interestingly, the crystallinity of the copolymer is much stronger on the ZnO layer, leading to a much improved maximum PCE of ∼8.2% when blended with PC₇₁BM in the inverted solar cell device. To our knowledge, this maximum PCE is among the highest of reported ladder-type D-A copolymers.[26,27]

## 2. EXPERIMENTAL SECTION

General experimental information on materials, device fabrication, and characterizations can be found in the Supporting Information.

**Synthesis of Monomers and Polymers.** *3,6-Dibromo-9,9-di(2-hexyldecyl)-9H-fluorene (1).* To a flask were added 3,6-dibromofluorene (3.24 g, 10.0 mmol), 2-hexyldecyl bromide (7.7 g, 25.0 mmol), tetrabutyl ammonium iodide (0.1 g), 10 mL of 50% NaOH solution, and 15 mL of DMSO. The mixture was heated at 100 °C under nitrogen overnight. After cooling to room temperature, the mixture was quenched with water and extracted with petroleum ether. The organic layer was dried over anhydrous magnesium sulfate and concentrated by rotary evaporation. The crude product was further purified by silica gel column chromatography using petroleum ether as the eluent to afford 6.41 g of pure product (83% yield). ¹H NMR (400 MHz, CDCl₃) δ (ppm):7.77 (s, 2H), 7.40 (d, J = 8.0 Hz, 2H), 7.24 (d, J = 8.1 Hz, 2H), 1.91 (d, J = 5.4 Hz, 4H), 1.10−0.63 (m, 60H), 0.45 (s, 2H). ¹³C NMR (100 MHz, CDCl₃) δ (ppm): 149.37, 142.11, 129.91, 125.59, 123.10, 120.88, 54.82, 44.87, 36.12, 34.68, 33.12, 31.93, 31.77, 29.63, 29.52, 29.36, 29.31, 25.88, 22.74, 22.68, 14.16, 14.12. MALDI-TOF MS for C₄₅H₇₂Br₂: calcd. 770.4; found, 770.4 (M⁺).

*3,6-Dimethylsulfide-9,9-di(2-hexyldecyl)-9H-fluorene (2).* A solution of 2.4 M n-BuLi (4.6 mL, 11.0 mmol) in THF was added dropwise to the solution of 3,6-dibromo-9,9-di(2-hexyldecyl)-9H-fluorene (1, 3.86 g, 5.0 mmol) in 200 mL of anhydrous THF at −78

**Scheme 1. Synthetic Route of DTTF and the Ladder-type D-A Copolymer PDTTF-DTBT**



PDTTF-DTBT    R=2-hexyldecyl
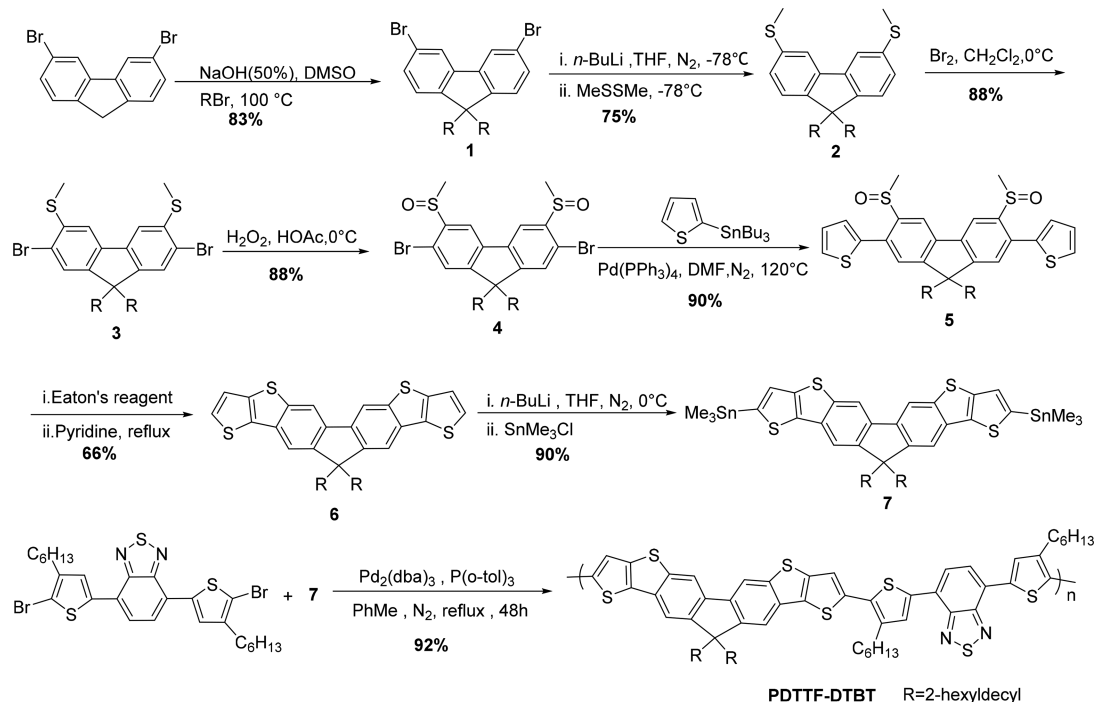
°C under nitrogen. After stirring for 30 min, 1.34 mL of dimethyl disulfide (15.0 mmol) was added into the mixture. The reaction mixture was then warmed up to room temperature and quenched by water. The resultant mixture was extracted with petroleum ether. The combined organics were dried over anhydrous magnesium sulfate. After the removal of the solvent by rotary evaporation, the crude product was further purified by silica gel column chromatography using petroleum ether–methylene dichloride (5/1, v/v) as the eluent to afford 2.65 g of the product (75% yield). $^1$H NMR (400 MHz, CDCl$_3$) δ (ppm):7.57 (d, J = 1.5 Hz, 2H), 7.24 (s, 2H), 7.18 (d, J = 9.3 Hz, 2H), 2.55 (s, 6H), 1.91 (d, J = 5.3 Hz, 4H), 1.25−0.81 (m, 60H), 0.69 (s, 2H). $^{13}$C NMR (100 MHz, CDCl$_3$) δ (ppm): 148.10, 141.47, 136.55, 125.84, 124.40, 118.38, 54.44, 44.97, 34.66, 33.12, 31.90, 31.76, 31.59, 29.67, 29.52, 29.32, 29.05, 25.83, 22.70, 22.64, 16.66, 14.10, 14.06, 11.39. MALDI-TOF MS for C$_{47}$H$_{78}$S$_2$: calcd. 706.6; found, 707.6 (M + H$^+$).

*2,7-Dibromo-9,9-di(2-hexyldecyl)-3,6-dimethylsulfide-9H-fluorene (3).* To a solution of 3,6-dimethylsulfide-9,9-di(2-hexyldecyl)-9H-fluorene (2, 2.50 g, 3.5 mmol) in 20.0 mL of CH$_2$Cl$_2$ was added in 0.1 g of iodine as the catalyst. Liquid bromine (0.35 mL, 7.0 mmol) was then added dropwise to the mixture at 0 °C. After the reaction finished, the resultant mixture was poured into diluted aqueous NaOH solution and extracted with CH$_2$Cl$_2$. The combined organic layer was dried over anhydrous magnesium sulfate and concentrated after the removal of the solvent by rotary evaporation. The crude product was further purified by silica gel column chromatography using petroleum ether−CH$_2$Cl$_2$ (5/1, v/v) as the eluent to afford 2.7 g of pure product (88% yield). $^1$H NMR (400 MHz, CDCl$_3$) δ (ppm): 7.51 (s, 2H), 7.44 (s, 2H), 2.59 (s, 6H), 1.90 (d, J = 5.1 Hz, 4H), 1.24−0.77 (m, 60H), 0.50 (s,2H). $^{13}$C NMR (100 MHz, CDCl$_3$) δ (ppm): 148.57, 139.93, 137.93, 128.62, 121.04, 116.86, 54.84, 44.53, 34.77, 33.21, 31.86, 31.75, 29.72, 29.52, 29.33, 25.93, 22.67, 16.30, 14.12, 14.08. MALDI-TOF MS for C$_{47}$H$_{76}$Br$_2$S$_2$: calcd. 862.4; found, 879.2 (M + NH$_4$$^+$).

*2,7-Dibromo-9,9-di(2-hexyldecyl)-3,6-bis(methylsulfinyl)-9H-fluorene (4).* 2,7-Dibromo-9,9-di(2-hexyldecyl)-3,6-dimethylsulfide-9H-fluorene (3, 0.87 g, 1.0 mmol) was dissolved in 10 mL of the mixture solvent of chloroform−acetic acid (1/1, v/v). 30% H$_2$O$_2$ (0.22 mL, 2.0 mmol) was then added into the mixture and stirred overnight. The reaction mixture was quenched by adding diluted NaOH solution and extracted with CH$_2$Cl$_2$. The combined organic layer was dried over

anhydrous magnesium sulfate and concentrated. The crude product was further purified by silica gel column chromatography using petroleum ether−acetone (5/1, v/v) as the eluent to afford 0.79 g of pure product (88% yield). $^1$H NMR (400 MHz, CDCl$_3$) δ (ppm): 8.40 (d, J = 2.4 Hz, 2H), 7.57 (s, 2H), 2.86 (d, J = 4.8 Hz, 6H), 2.01 (s, 4H), 1.37−1.02 (m, 26H), 0.95−0.64 (m, 34H), 0.47 (s, 2H). $^{13}$C NMR (100 MHz, CDCl$_3$), δ (ppm): 154.63, 145.03, 140.14, 128.57, 117.71, 117.06, 116.97, 55.96, 42.06, 34.58, 33.28, 31.71, 31.57, 29.58, 29.37, 29.17, 25.87, 22.50, 13.95. MALDI-TOF MS for C$_{47}$H$_{76}$-Br$_2$O$_2$S$_2$: calcd. 897.1; found, 897.2 (M$^+$).

*2,7-Bis(thiophen-2-yl)-9,9-di(2-hexyldecyl)-3,6-bis(methylsulfinyl)-9H-fluorene (5).* 2,7-Dibromo-9,9-di(2-hexyldecyl)-3,6-bis-(methylsulfinyl)-9H-fluorene (4, 1.36 g, 1.5 mmol), Pd(PPh$_3$)$_4$ (46 mg, 0.044 mmol), 2-(tributylstannyl)thiophene (1.42 g, 3.8 mmol), and 10.0 mL of anhydrous DMF were added into a flask under nitrogen. The reaction was heated to 100 °C and stirred for 24 h. The mixture was washed with water and extracted with CH$_2$Cl$_2$. The combined organic layer was dried over anhydrous magnesium sulfate and concentrated. The crude product was further purified by silica gel column chromatography using petroleum ether/acetone (10/1, v/v) as the eluent to afford 1.3 g of the pure product (90% yield). $^1$H NMR (400 MHz, CDCl$_3$) δ (ppm): 8.62 (d, J = 4.1 Hz, 2H), 7.47 (d, J = 7.2 Hz, 4H), 7.26−7.09 (m, 4H), 2.56 (d, J = 16.2 Hz, 6H), 2.06 (s, 4H), 1.42−0.64 (m, 60H), 0.54 (s, 2H). $^{13}$C NMR (100 MHz,CDCl$_3$) δ (ppm): 153.23, 144.36, 141.03, 138.99, 138.92, 130.29, 130.18, 127.70, 127.52, 126.95, 126.61, 116.08, 55.77, 42.28, 34.91, 31.69, 31.52, 29.34, 29.14, 25.92, 22.46, 22.42, 13.92. MALDI-TOF MS for C$_{55}$H$_{82}$Br$_2$O$_2$S$_4$: calcd. 903.5; found, 903.3 (M$^+$).

*12,12-Bis(2-hexyldecyl)-12H-ditheno[2′,3′:4,5]thieno[3,2-b:2′,3′-h]fluorene (6).* To a flask were added 2,7-bis(thiophen-2-yl)-9,9-di(2-hexyldecyl)-3,6-bis(methylsulfinyl)-9H-fluorene (5, 1.63 g, 1.8 mmol) and 10 mL of Eaton's reagent; the mixture was stirred in the dark for 48 h at room temperature. The reaction mixture was then added dropwise into ice water and extracted with chloroform. The combined organic layer was dried over anhydrous magnesium sulfate and concentrated. The crude product was then added into 40 mL of pyridine and refluxed for 12 h. The solvent was then removed by rotary evaporation. The crude product was purified by silica gel column chromatography using petroleum ether as the eluent to afford 1.1 g of pure product (66% yield). $^1$H NMR (400 MHz, CDCl$_3$) δ

(ppm): 8.17 (s, 2H), 7.80 (s, 2H), 7.49 (d, *J* = 5.1 Hz, 2H), 7.32 (d, *J* = 5.1 Hz, 2H), 2.13 (s, 4H), 1.25(s, 12H), 0.94−0.61 (br, 50H). $^{13}$C NMR (100 MHz, CDCl$_3$) $\delta$ (ppm): 148.32, 142.04, 138.36, 138.05, 134.96, 131.65, 127.31, 120.42, 116.38, 114.60, 54.23, 45.78, 34.69, 33.19, 31.74, 29.70, 29.54, 29.29, 25.87, 22.65, 22.56, 14.12, 13.88. MALDI-TOF MS for C$_{53}$H$_{74}$S$_4$: calcd 838.4; found, 839.1 (M$^+$).

*2,9-Bis(trimethyltin)-12,12-bis(2-hexyldecyl)-12H-dithieno-[2′,3′:4,5]thieno[3,2-b:2′,3′-h]fluorene (7).* A solution of 2.4 M *n*-BuLi (0.9 mL, 2.16 mmol) in hexane was added dropwise to the solution of 12,12-bis(2-hexyldecyl)-12H-dithieno[2′,3′:4,5]thieno[3,2-b:2′,3′-h]fluorene (6, 0.84 g, 1.0 mmol) in 20 mL of anhydrous THF at 0 °C under nitrogen. After stirring for 1 h, a solution of 1 M Me$_3$SnCl (3 mL, 3.0 mmol) in hexane was added into the mixture. After 2 h, the reaction was quenched with water and extracted with CH$_2$Cl$_2$. The combined organic layer was dried over anhydrous magnesium sulfate. The removal of the solvent under reduced pressure afforded 1.05 g of the pure product (90% yield). $^1$H NMR (400 MHz, CDCl$_3$) $\delta$ (ppm): 8.13 (s, 2H), 7.78 (s, 2H), 7.34(s, 2H), 2.11(s, 4H), 1.13−0.62 (m, 62H), 0.51−0.37(m, 18h). $^{13}$C NMR (100 MHz, CDCl3) $\delta$ (ppm): 148.23, 142.43, 141.52, 141.49, 140.80, 139.87, 138.28, 131.29, 127.46, 116.58, 114.70, 54.17, 45.82, 34.73, 34.67, 33.17, 31.86, 31.75, 29.30, 25.90, 22.66, 22.62, 14.15, 13.95, −8.19. MALDI-TOF MS for C$_{59}$H$_{90}$S$_4$Sn$_2$: calcd. 1165.3; found, 1165.3 (M$^+$).

*Poly([12,12-bis(2-hexyldecyl)-12H-dithieno[2′,3′:4,5]thieno[3,2-b:2′,3′-h]fluorene-2,9-diyl]-alt-[4,7-bis(4-hexylthiophen-2-yl)benzo-[c][1,2,5]thiadiazole-5,5-diyl]) (PDTTF-DTBT).* To a two-neck round-bottom flask were added **7** (0.35 g, 0.30 mmol), 4,7-bis(5′-bromo-4′-hexylthiophen-2-yl)benzo[c][1,2,5]thiadiazole (0.19g, 0.30 mmol), Pd$_2$(dba)$_3$ (0.084 g, 0.092 mmol), P(o-tol)$_3$ (0.017 g, 0.056 mmol), and 15.0 mL of anhydrous toluene under nitrogen. After being purged with nitrogen for 10 min, the reaction mixture was heated to reflux for 48 h with stirring. Then the reaction mixture was cooled down to room temperature and precipitated by adding dropwise into 100 mL of methanol under stirring. The solid was collected by filtration, and then the crude product was purified by Soxhlet extraction with methanol, acetone, hexane, CH$_2$Cl$_2$, and chloroform sequentially. The fraction in chloroform was concentrated and reprecipitated in 10 mL of methanol, and then the resulting solid was filtered and dried under vacuum to afford 0.36 g of the target polymer (92% yield). GPC: $M_n$ = 40.80 kg mol$^{-1}$, $M_w$ = 104.96 kg mol$^{-1}$, PDI = 2.57. A resolvable $^1$H NMR spectrum of the copolymer was not obtained due to its strong aggregation in the CDCl$_3$ solution for NMR testing.

## 3. RESULTS AND DISCUSSION

**Synthesis.** The synthesis of the ladder-type heterohepta-cene **6** with the skeleton of 12H-dithieno[2′,3′:4,5]thieno[3,2-b:2′,3′-h]fluorene and the D-A copolymer **PDTTF-DTBT** is outlined in Scheme 1. 3,6-Dibromofluorene was dialkylated with 2-hexyldecyl bromide in the presence of NaOH as the base and tetrabutyl ammonium iodide as the catalyst in dimethyl sulfoxide to afford **1**. The two bulky 2-hexyldecyl chains were introduced to promote the solubility and processability of the resulting D-A copolymer. Compound **2** was synthesized by dilithiation of **1** with 2.1 equiv of *n*-BuLi, followed by quenching with dimethyl disulfide. Regioselective bromination at 2- and 7-positions of **2** was achieved by using bromine to give **3**, which was subsequently oxidized with hydrogen peroxide in acetic acid to give **4**. The Stille coupling reaction between **4** and 2-(tributylstannyl)thiophene was carried out in DMF with Pd(PPh$_3$)$_4$ as the catalyst to give compound **5**. Afterward, double intramolecular ring closure was induced by treating **5** with Eaton's reagent to afford target heteroheptacene **6** as a white solid. The heteroheptacene **6** was obtained in an overall yield of approximately 30% from 3,6-dibromofluorene. The distannylation of **6** was further achieved through a standard stannylation of compound **6** to give monomer **7** in excellent yield. The target D-A copolymer **PDTTF-DTBT** was

then synthesized through the Stille polymerization of monomer **7** and 4,7-bis(5-bromo-4-hexylthiophen-2-yl)benzo[c][1,2,5]-thiadiazole. Soxhlet purification of the crude product afforded the D-A copolymer from CHCl$_3$ fraction with high solubility in common organic solvents (e.g., CHCl$_3$, toluene, chlorobenzene, and o-dichlorobenzene) at room temperature, which guaranteed the solution processability for device fabrication. Gel permeation chromatography (GPC) of the purified polymer in tetrahydrofuran (THF) determined a number-average molecular weight ($M_n$) of 40.80 kg mol$^{-1}$ and weight-average molecular weight ($M_w$) of 104.96 kg mol$^{-1}$ with a dispersity (PDI) of 2.57. **PDTTF-DTBT** exhibited good thermal stability with a decomposition temperature ($T_d$, corresponding to 5% weight loss) of 380 °C as determined via thermogravimetric analysis (TGA) (Figure S1).

**Optical and Electrochemical Properties.** Depicted in Figure 1 are normalized UV−vis absorption spectra of **PDTTF-**
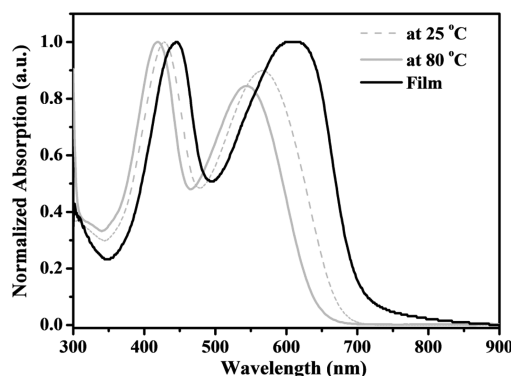


**Figure 1.** Normalized UV−vis spectra of **PDTTF-DTBT** in o-DCB (2 × 10$^{-5}$ g mL$^{-1}$) at 25 and 80 °C and in thin film (cast from 10 mg mL$^{-1}$ solution in o-DCB).

**DTBT** in o-DCB solution with the fixed concentration of 2 × 10$^{-5}$ g mL$^{-1}$ at 80 °C and in film. As can be seen from the temperature dependent absorption spectra in solution (Figure S2), a hypochromic shift of ~25 nm can be observed as the temperature increases from room temperature to 80 °C. Such apparent hypochromic shift indicates a strong tendency of **PDTTF-DTBT** to aggregate even in diluted solution. The spectra both in solutions and in film display similar dual-band absorption characteristic of a D-A copolymer. The higher energy band absorbance is attributed to the $\pi$−$\pi$* transition of the heptacyclic $\pi$-conjugated backbone, while the lower energy band at longer wavelength comes from the intramolecular charge transfer (ICT) between electron-rich **DTTF** and electron-deficient benzothiadiazole moieties. The film absorption coefficient curve of **PDTTF-DTBT** indicates a maximum absorption coefficient close to 6.0 × 10$^4$ cm$^{-1}$ in the absorption range. In the film state, the absorption maximum on the ICT band is remarkably red-shifted by around 70 nm relative to the solution at the temperature of 80 °C due to strong aggregation induced by interchain interactions in the solid phase. As will be detailed in the morphology section, this strong aggregation observed by the thin film absorption implies an appreciable amount of molecular ordering in the solid state. This ordered packing of polymer chains would benefit the $J_{sc}$ and the charge carrier (i.e., hole) mobility within solar cell devices. Please note that such notable bathochromic shift was unprecedentedly observed from D-A copolymers based on ladder-type multi-cyclic aromatics bearing multiple tetrahedral carbon bridges

within the conjugated backbones.[26−28] These optical behaviors confirm that attaching two thienothiophenes to the fluorene center to extend $\pi$-conjugation does improve intermolecular interactions as we originally anticipated. The HOMO energy level ($-5.36$ eV) of **PDTTF-DTBT** was calculated from the oxidation onset potential (0.56 V vs ferrocene) determined by cyclic voltammetry as shown in Figure S3. Taking into account the optical band gap (1.72 eV) derived from the absorption onset (720 nm) in the film, the LUMO energy level of **PDTTF-DTBT** was estimated to be $-3.64$ eV according to $E_{LUMO} = (E_{HOMO} + E_{g,opt})$ eV.

**Photovoltaic Properties.** To evaluate the photovoltaic performance of **PDTTF-DTBT** as the donor material, we chose $PC_{71}BM$ as the acceptor, and fabricated bulk hetero-junction polymer solar cells with both conventional (ITO/PEDOT:PSS/Polymer:$PC_{71}BM$/Ca/Al) and inverted (ITO/ZnO/Polymer:$PC_{71}BM$/MoO$_3$/Ag) architectures. The energy level diagrams of the electronic materials within both device architectures are depicted in Figure S4, which clearly indicates energetically favorable electron transfer and charge transport in either device architecture. We first investigated the weight ratio of **PDTTF-DTBT** vs $PC_{71}BM$ (1:1, 1:2, 1:3) with a fixed concentration of 10 mg mL$^{-1}$ for **PDTTF-DTBT** in $o$-DCB. The film thickness of the BHJ blends was also varied as part of the device optimization procedure. The device data are summarized in Tables S1 and S2 as well as corresponding current density−voltage ($J$−$V$) curves in Figures S5 and S6. The optimal weight ratio of **PDTTF-DTBT**:$PC_{71}BM$ was determined to be 1:2. The solvent additive of DIO was further applied to the blend of **PDTTF-DTBT**:$PC_{71}BM$ (1:2, w/w) to enhance the performance in both device architectures. The photovoltaic performances of solar cells fabricated with various DIO concentrations are summarized in Tables S3 and S4, while the $J$−$V$ curves of typical solar cells are shown in Figures S7 and S8. It can be found that the maximal photovoltaic performance was reached with 1% DIO (v/v) in $o$-DCB as the processing condition, in both the conventional and the inverted devices. $J$−$V$ characteristics of the optimized devices under AM 1.5G solar irradiation with a light intensity of 100 mW cm$^{-1}$ are shown in Figure 2a, and the corresponding device parameters are summarized in Table 1. Specifically, the conventional device obtained a maximum PCE of 5.93% with a $V_{oc}$ of 0.83 V, a $J_{sc}$ of 13.76 mA cm$^{-2}$, and an FF of 53.0%. Encouragingly, the maximum PCE was dramatically improved to 8.17% for the inverted device with a $V_{oc}$ of 0.86 V, a $J_{sc}$ of 14.55 mA cm$^{-2}$, and an FF of 65.0%. The external quantum efficiency (EQE) spectra of BHJ devices both in conventional and in inverted architectures are shown in Figure 2b. Both types of solar cells yield broad EQE spectra from 300 to 750 nm. The EQE value approaches 80% over the wavelength range of 400 and 550 nm for the inverted device. In the wavelength range of 370 and 640 nm, the EQE of the inverted device exceeds that of the conventional one, confirming the higher $J_{sc}$ of the inverted device as measured. For both types of devices, the $J_{sc}$ values calculated from the EQE spectra are consistent with the $J_{sc}$ values obtained from direct photo $J$−$V$ measurements, 12.67 mA cm$^{-2}$ for the conventional device and 13.82 mA cm$^{-2}$ for the inverted device (right axis in Figure 2), which confirms the accuracy of the reported PCE values.

**Film Surface Morphology, Molecular Packing, and Phase Separation.** Comparing the device characteristics of the conventional device with those of the inverted reveals that the main improvement of the efficiency is from the FF ($\sim$30%
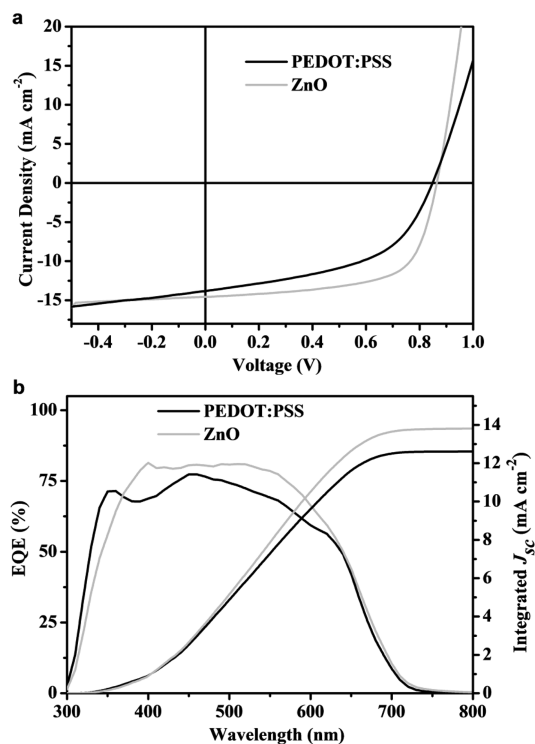


**Figure 2.** (a) Typical $J$−$V$ curves of solar cells with **PDTTF-DTBT**:$PC_{71}BM$ and (b) corresponding EQE spectra and integrated $J_{sc}$ curves in conventional and inverted device configurations, respectively.

increase) and the $J_{sc}$ ($\sim$7% increase). This observation implies that there is less charge recombination and more efficient charge transport and collection in the inverted devices. Since the film morphology plays an important role in affecting the charge transport/recombination properties, we then investigated the surface morphology of the **PDTTF-DTBT**:$PC_{71}BM$ blend by tapping-mode atomic force microscopy (AFM). Compared with the conventional device (Figure S9), the **PDTTF-DTBT**:$PC_{71}BM$ blend in the inverted device presented a well-mixed interpenetrating network with smaller aggregated domain sizes and smoother surface roughness (the root-mean-square roughness values for the conventional and inverted devices are 3.4 and 2.0 nm, respectively), suggesting that the BHJ blend in the inverted device has favorable morphology features for efficient charge separation and transporting.

Grazing incidence wide-angle X-ray scattering (GIWAXS) was next employed to investigate the crystallization behavior of the neat polymer (**PDTTF-DTBT**) and the **PDTTF-DTBT**:$PC_{71}BM$ blend (Figure S10) on both PEDOT:PSS and ZnO layers. The composition and deposition conditions of **PDTTF-DTBT**:$PC_{71}BM$ blends for the GIWAXS study were identical to those of optimized devices for either conventional or inverted architectures. Silicon substrates were used instead of ITO to reduce the background scattering. The intensity profiles of the pure and blend films along in-plane and out-of-plane directions are plotted in Figure 3 with the corresponding two-dimensional GIWAXS patterns presented in Figure S10. For the neat films, a much obvious and intense lamellar stacking peak of **PDTTF-DTBT** is observed at the low $q$ region ($\sim$0.16 Å$^{-1}$) on the ZnO layer, indicating the formation of high crystallinity polymer phases with a particularly large lamellar $d$-spacing of $\sim$39.3 Å resulting from the incorporation of two

**Table 1. Photovoltaic Properties of the Conventional and Inverted Devices with 1% DIO**

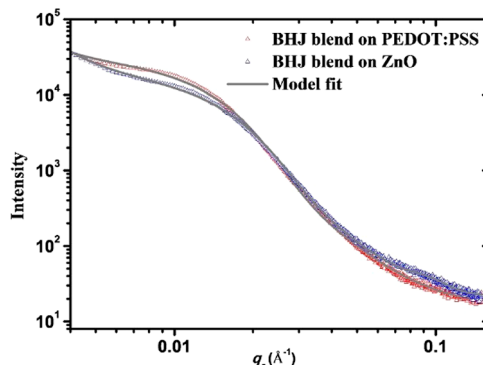| device configuration | $V_{oc}$ [V] | $J_{sc}$ [mA cm$^{-2}$] | FF | PCE [%] | $\mu_h$ [cm$^2$ V$^{-1}$ S$^{-1}$] | $\mu_e$ [cm$^2$ V$^{-1}$ S$^{-1}$] |
|---|---|---|---|---|---|---|
| conventional | 0.83 | 13.76 (12.67)[a] | 0.51 | 5.93 (5.68)[b] | $2.21 \times 10^{-4}$ | |
| inverted | 0.86 | 14.55 (13.82)[a] | 0.65 | 8.17 (7.88)[b] | | $1.08 \times 10^{-4}$ |

[a]Calculated from EQE spectra as shown in Figure 2b. [b]Parentheses values are for average PCEs (over 20 devices).
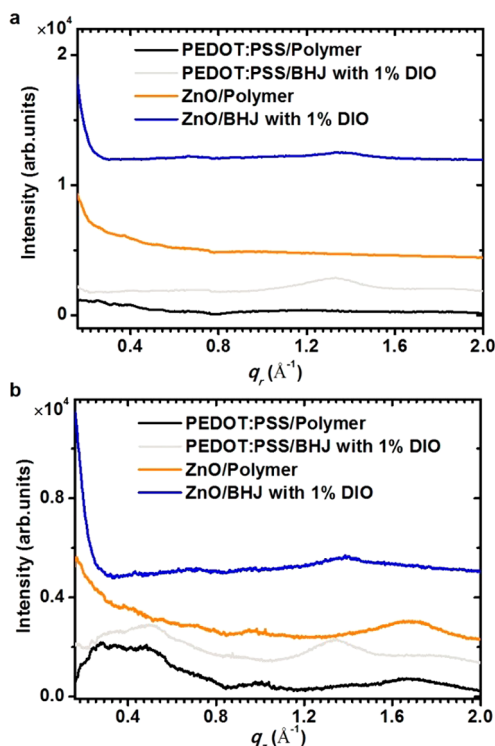


**Figure 3.** In-plane (a) and out-of-plane (b) GIWAXS profiles of films of the pristine polymer and **PDTTF-DTBT**:PC$_{71}$BM BHJ blends with 1% DIO spun-cast on PEDOT:PSS and ZnO layers, respectively.



**Figure 4.** GISAXS in-plane profiles of the BHJ blend films on PEDOT:PSS and ZnO layers and their model fittings.

long branched side alkyl chains (2-hexydecyl) bonded on the tetrahedral carbon bridge at the 12,12-position of the **DTTF** backbone. Note here, the lamellar peak is partially blocked by the beam stop due to the small $q$ value, making it difficult to identify the peak position. Furthermore, the pure films exhibited a broad reflection at 1.69 Å$^{-1}$ ($d$ = 3.72 Å) on the ZnO layer and 1.66 Å$^{-1}$ ($d$ = 3.78 Å) on the PEDOT:PSS layer in the out-of-plane direction, corresponding to a preferential face-on oriented $\pi-\pi$ stacking of conjugated backbones. In the BHJ blend films where the polymer packing is disturbed by the introduction of PC$_{71}$BM, the lamellar peak can only be observed from the film on the ZnO layer with the addition of DIO additive.

Grazing incidence small-angle X-ray scattering (GISAXS) was further applied to investigate the in-plane nanoscale phase separation information via effective surface approximation.[30,31] The 2D GISAXS patterns are shown in Figure S11. Figure 4 presents the intensity profiles of the BHJ blend films in the $q_r$ direction at the reflected beam position, while the data of the neat polymer film on both layers are provided in Figure S12. The BHJ blend film exhibits an obvious shoulder on both PEDOT:PSS and ZnO layers, implying the presence of structure order. The observed shoulders could result from the scattering of aggregated PC$_{71}$BM clusters due to the effect of strong polymer:PC$_{71}$BM phase separation as found in other polymer:PC$_{71}$BM blends.[30−32] To quantify and compare the

phase separation behavior of the BHJ blends on PEDOT:PSS and ZnO layers, respectively, the GISAXS profiles were fitted with the Debye−Anderson−Brumberger (DAB) model for amorphous phases with dispersed PC$_{71}$BM molecules and the hard-sphere model for aggregated PC$_{71}$BM clusters and polymer domains. The average sizes of the crystalline polymer domain $2R_{g-polymer}$, amorphous polymer:PC$_{71}$BM mixture domain $\xi$, and clustered PC$_{71}$BM domains $2R_{g-PC_{71}BM}$ can be roughly estimated.[30−33] For the BHJ blend on the PEDOT:PSS layer, the domain sizes of the amorphous phase $\xi$ and the clustered PC$_{71}$BM phase $2R_{g-PC_{71}BM}$ are around 57.9 and 22.6 nm, respectively, while the polymer domain is 3.0 nm. Nevertheless, the domain of amorphous phase $\xi$ and clustered PC$_{71}$BM phase $2R_{g-PC_{71}BM}$ are 48.4 and 20.4 nm, respectively, for the BHJ film on the ZnO layer with the polymer domain increased to 6.0 nm. The decrease in amorphous phase size could be beneficial to the charge collection from this region. The clustered PC$_{71}$BM phase size is smaller for the film on the ZnO layer, consistent with the AFM measurement results. The size of the polymer domain grew slightly on the ZnO layer, becoming closer to the theoretical exciton diffusion length in organic materials (∼10 nm), which might reduce the unwanted recombination caused by too small polymer domain size observed for the film on the PEDOT:PSS layer. Overall, the higher crystallinity, tighter $\pi-\pi$ stacking, and appropriate phase separation behaviors of the BHJ film on the ZnO layer reasonably explain the enhanced charge separation and transport as described below to reach higher $J_{sc}$, FF, and PCE in the inverted device.

**Charge Transport, Recombination, and Collection.** Since morphological study of these thin films only offers qualitative evidence to the observed difference in device characteristics between the conventional and inverted devices, we then further investigated charge transport, charge carrier generation, and charge recombination properties to search for more quantitative causes. To this end, we first measured the electron ($\mu_e$) and hole ($\mu_h$) mobilities of **PDTTF-DTBT**:PC$_{71}$-BM blends in electron- and hole-only devices (i.e., ITO/PEDOT:PSS/**PDTTF-DTBT**:PC$_{71}$BM/MoO$_3$/Ag and ITO/
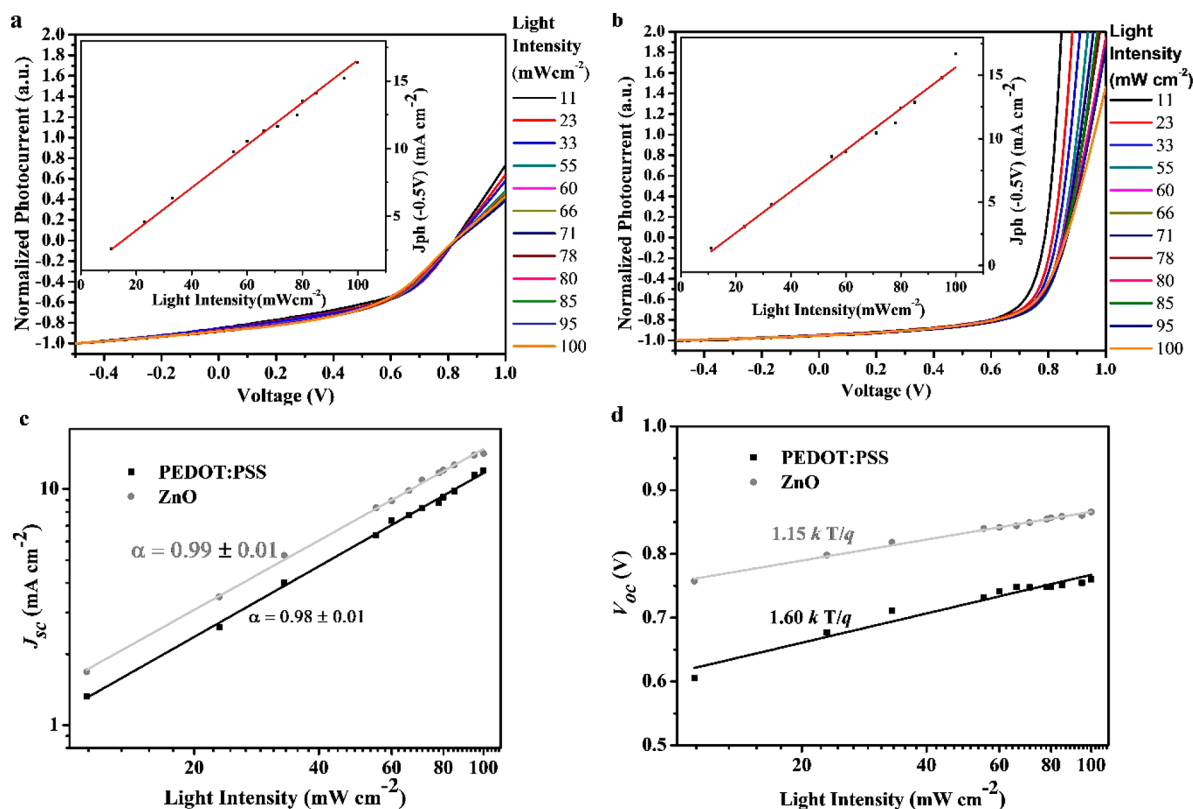
**Figure 5.** Photocurrent normalized to reverse saturation photocurrent at −0.5 V plotted against incident light intensity of **PDTTF-DTBT**:PC$_{71}$BM solar cell devices with conventional (a) and inverted (b) architectures, respectively (Inset: the current densities at −0.5 V plotted against light intensities ranging from 11 to 100 mW cm$^{-2}$). The dependence of measured $J_{sc}$ (c) and $V_{oc}$ (d) on light intensity of **PDTTF-DTBT**:PC$_{71}$BM solar cell devices with conventional and inverted architectures.

ZnO/**PDTTF-DTBT**:PC$_{71}$BM/Ca/Al, respectively) via the space charge limited current (SCLC) method. Fitting the data in Figure S13 reveals that the hole mobility in the conventional device is around $2.21 \times 10^{-4}$ cm$^2$ V$^{-1}$ S$^{-1}$, whereas the electron mobility in the inverted device is around $1.08 \times 10^{-4}$ cm$^2$ V$^{-1}$ S$^{-1}$ (Table 1). Please note that $\mu_e$ and $\mu_h$ of **PDTTF-DTBT**:PC$_{71}$BM blends can only be obtained from the inverted and conventional devices separately, because of the distinctively different molecular packing order of **PDTTF-DTBT**:PC$_{71}$BM blend films on ZnO and PEDOT:PSS layers, respectively. For this reason, we cannot make a direct comparison on charge transport between the conventional and inverted devices. Nevertheless, we argue that both electron and hole mobilities in the inverted device could be improved due to the above-mentioned beneficial ordering of the BHJ blend on the ZnO layer.

We next investigated the variation of photogenerated current ($J_{ph}$, defined by subtracting dark current density $J_{dark}$ from total current density $J$ under illumination at applied voltages) as a function of the incident light intensity ($P_{light}$) at applied voltages (Figure S14) in order to gain insight into the charge recombination mechanisms within two types of devices.[34−36] As can be seen from the insets of Figure 5a,b, the $J_{ph}$ becomes linearly variable to $P_{light}$ at applied voltage around −0.5 V in both conventional and inverted devices, indicating the reverse saturation photocurrent ($J_{ph,sat}$) at −0.5 V. Normalizing $J_{ph}$ to $J_{ph,sat}$ under illuminations covering an intensity range from 100 to 11 mW cm$^{-2}$ afforded a set of normalized photocurrents, defined as the charge collection probability ($P_c$) at applied voltages as indicated in Figure 5a,b. For the conventional device

(Figure 5a), a subtle divergence of $P_c$ vs voltage curves under different light intensity can be observed from negative applied voltages of −0.2 V to approximately 0.55 V, which is close to the maximum power point (MPP), indicating a slight dependence of the charge collection probability ($P_c$) on light intensity ($P_{light}$). This dependence of $P_c$ on the light intensity remains when the applied voltage approaches open-circuit voltage from the MPP. These data indicate that bimolecular recombination dominates at the applied voltages from the short-circuit to near the MPP for the conventional device.[35,36] However, as shown in Figure 5b, the shapes of $P_c$ curves are very different in the inverted device. Specifically, the $P_c$ curves on different light intensity overlap over a wide range of applied voltages from −0.5 to ∼0.65 V (MPP), implying that the recombination is primarily controlled by a monomolecular mechanism from the short-circuit condition to near the MPP. It is also worth noting that the $P_c$ curves beyond the MPP evolve to be strongly light intensity dependent, largely due to the attenuated effective internal field.

We further attempted to quantify the charge recombination losses of two types of devices via probing the relationship between the device $J$−$V$ characteristics and the incident light intensity ($P_{light}$). First, we plotted the dependence of $J_{sc}$ on $P_{light}$ according to the relationship of $J_{sc} \propto (P_{light})^\alpha$ (Figure 5c), where the value of the power law scaling exponent $\alpha$ indicates the strength of the bimolecular recombination at the short-circuit condition. The closer the $\alpha$ approaches unity, the weaker the bimolecular recombination is. On the other hand, we plotted the dependence of $V_{oc}$ versus the logarithm of $P_{light}$, following $V_{oc} \propto (nkT/q)/\ln(P_{light})$ (Figure 5d) to determine the $n$ value,

where $k$ is Boltzmann constant, $T$ is the temperature in Kelvin, and $q$ is the elementary charge. A value of $n$ close to unity would indicate that the bimolecular recombination dominates the recombination loss. When additional Shockley—Read—Hall (SRH) or trap-assisted recombination is involved, the competition with the bimolecular recombination would lead to an increased $n$ (i.e., $n > 1$).[34,35,37−39] In our devices, a slightly larger $\alpha$ (0.99) was obtained for the inverted device than that of the conventional one (0.98), indicating that bimolecular recombination loss at short-circuit condition is relatively small in both types of devices. This is in agreement with the analysis of the $P_c$ curves at various $P_{light}$ in Figure 5a,b. On the other hand, fitting the curves in Figure 5d offers an $n$ of 1.15 for the inverted device, whereas an $n$ of 1.60 was obtained for the conventional device. This result indicates a significantly reduced trap-assisted recombination in the inverted device at open-circuit condition. The suppressed SRH recombination can be ascribed to the much improved molecular packing and phase separation in **PDTTF-DTBT**:PC$_{71}$BM blend film on the ZnO layer as discussed above and also the likely reduction of the density of interfacial traps between the BHJ blend and the ZnO layer.

Lastly, we experimentally determined the maximum photo-induced carriers generation rate ($G_{max}$) in both types of devices under AM 1.5G illumination.[37,38,40] Figure 6 reveals $J_{ph}$ versus
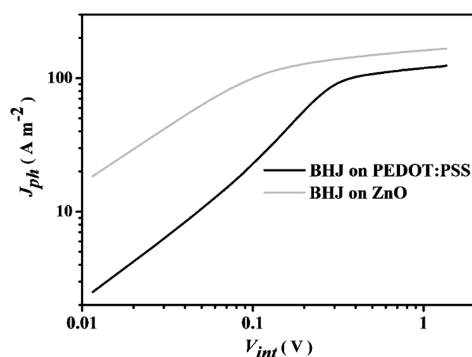


**Figure 6.** Photocurrent density as a function of internal voltage for the solar cell devices with the BHJ blend on PEDOT:PSS or ZnO layer.

the internal voltage ($V_{int}$) of the devices on the PEDOT:PSS layer and on the ZnO layer, respectively. $V_{int}$ is determined as $V_{int} = V_{bi} - V_{app}$, where $V_{bi}$ is the built-in voltage, which refers to the voltage at which $J_{ph}$ is zero, and $V_{app}$ is the applied voltage. $J_{ph}$ increases in proportion to the voltage at low $V_{int}$, but saturates at high $V_{int}$ (around 1.5 V and above) where the internal field is large enough to sweep out all carriers to the electrodes. The value of $G_{max}$ of the device with PEDOT:PSS is calculated to be $8.34 \times 10^{27}$ m$^{-3}$ s$^{-1}$ ($J_{ph, sat} = 124.2$ A m$^{-2}$), whereas the $G_{max}$ of the device with ZnO increases to $1.04 \times 10^{28}$ m$^{-3}$ s$^{-1}$ ($J_{ph, sat} = 166.8$ A m$^{-2}$), a significantly higher value. We also examined the charge collection probability $P_c$ with respect to $V_{int}$ under AM 1.5G illumination for both types of solar cells. As shown in Figure S14, $P_c$ of the inverted device is higher than that of the conventional one across the whole range from the short circuit to the open-circuit condition. Specifically, the $P_c$ increases from 94.0% to 95.4% at the short-circuit condition by switching the device architecture from the conventional to the inverted one. Moreover, the increase in $P_c$ is more significant at low $V_{int}$ (high applied voltage). Thus, the charge collection was improved in the inverted device,

resulting in the enhancement of $J_{sc}$ compared to the conventional device. The suppressed SRH recombination at open-circuit condition and the high charge collection probability at short-circuit condition lead to an increased FF for the inverted device.

## 4. CONCLUSIONS

In summary, we have designed and synthesized a structurally well-defined novel electron-donating building block, 12H-dithieno[2′,3′:4,5]thieno[3,2-b:2′,3′-h]fluorene (**DTTF**), which was copolymerized with 4,7-bis(4-hexylthiophen-2-yl)-benzo[c][1,2,5]thiadiazole (**DTBT**) to construct a D-A copolymer (**PDTTF-DTBT**). **PDTTF-DTBT** exhibits a medium optical band gap of 1.72 eV and a low-lying HOMO level of −5.36 eV. We find that flanking two thienothiophenes by the fluorene center to extend the conjugated backbone in **DTTF** leads to strong intermolecular interactions of the copolymer without sacrificing solution processability. Blending the copolymer with PC$_{71}$BM as BHJ film on the PEDOT:PSS layer in the conventional solar cell device yielded a maximum PCE of 5.93% with a $V_{oc}$ of 0.83 V, a $J_{sc}$ of 13.76 mA cm$^{-2}$, and an FF of 53.0%. Notably, the maximum PCE was dramatically improved to 8.17% for the inverted device with the BHJ film on the ZnO layer, with a $V_{oc}$ of 0.86 V, a $J_{sc}$ of 14.55 mA cm$^{-2}$, and an FF of 65.0%. The enhancements of $J_{sc}$ and FF in the inverted device can be mainly attributed to the improvement of the packing order and appropriate phase separation of both the copolymer and PC$_{71}$BM in the BHJ blend on the ZnO layer, which reduced charge recombination and improved charge transport and collection probability. These desirable features advocate this new building block as a promising structural candidate for novel polymers on optoelectronic applications. The results also demonstrate that it is an effective strategy to incorporate a single tetrahedral carbon bridge to the molecular center of ladder-type heteroacenes with heavily extended $\pi$-conjugation to prepare D-A copolymers toward highly efficient PSCs.

## ■ ASSOCIATED CONTENT

### Ⓢ Supporting Information

The Supporting Information is available free of charge on the ACS Publications website at DOI: 10.1021/acsami.7b12142.

> General information on materials, TGA, temperature dependent UV−vis absorption spectra, cyclic voltammo-gram curve of the copolymer, detailed photovoltaic performance optimization, AFM images, GIWAXS and GISAXS patterns, incident light intensity dependent device performance (PDF)

## ■ AUTHOR INFORMATION

### Corresponding Authors

*E-mail: shengqiang@whut.edu.cn (S.X.).
*E-mail: xhlu@phy.cuhk.edu.hk (X.L.).
*E-mail: wyou@unc.edu (W.Y.).

### ORCID Ⓘ

Shengqiang Xiao: 0000-0001-7644-8491
Wei You: 0000-0003-0354-1948

### Notes

The authors declare no competing financial interest.

## ■ REFERENCES

(1) Bin, H.; Gao, L.; Zhang, Z.-G.; Yang, Y.; Zhang, Y.; Zhang, C.; Chen, S.; Xue, L.; Yang, C.; Xiao, M.; Li, Y. 11.4% Efficiency Non-Fullerene Polymer Solar Cells with Trialkylsilyl Substituted 2D-Conjugated Polymer as Donor. *Nat. Commun.* **2016**, *7*, 13651.

(2) Huang, J.; Carpenter, J. H.; Li, C.-Z.; Yu, J.-S.; Ade, H.; Jen, A. K. Y. Highly Efficient Organic Solar Cells with Improved Vertical Donor–Acceptor Compositional Gradient Via an Inverted Off-Center Spinning Method. *Adv. Mater.* **2016**, *28*, 967–974.

(3) Yao, H.; Chen, Y.; Qin, Y.; Yu, R.; Cui, Y.; Yang, B.; Li, S.; Zhang, K.; Hou, J. Design and Synthesis of a Low Bandgap Small Molecule Acceptor for Efficient Polymer Solar Cells. *Adv. Mater.* **2016**, *28*, 8283–8287.

(4) Zhao, J.; Li, Y.; Yang, G.; Jiang, K.; Lin, H.; Ade, H.; Ma, W.; Yan, H. Efficient Organic Solar Cells Processed from Hydrocarbon Solvents. *Nat. Energy* **2016**, *1*, 15027.

(5) Li, H.; He, D.; Mao, P.; Wei, Y.; Ding, L.; Wang, J. Additive-Free Organic Solar Cells with Power Conversion Efficiency over 10%. *Adv. Energy Mater.* **2017**, *7*, 1602663.

(6) Hu, Z.; Ying, L.; Huang, F.; Cao, Y. Towards a Bright Future: Polymer Solar Cells with Power Conversion Efficiencies over 10%. *Sci. China: Chem.* **2017**, *60*, 571–582.

(7) Dou, L.; You, J.; Hong, Z.; Xu, Z.; Li, G.; Street, R. A.; Yang, Y. 25th Anniversary Article: A Decade of Organic/Polymeric Photovoltaic Research. *Adv. Mater.* **2013**, *25*, 6642–6671.

(8) Li, Y. Molecular Design of Photovoltaic Materials for Polymer Solar Cells: Toward Suitable Electronic Energy Levels and Broad Absorption. *Acc. Chem. Res.* **2012**, *45*, 723–733.

(9) Liu, C.; Wang, K.; Gong, X.; Heeger, A. J. Low Bandgap Semiconducting Polymers for Polymeric Photovoltaics. *Chem. Soc. Rev.* **2016**, *45*, 4825–4846.

(10) Lu, L.; Zheng, T.; Wu, Q.; Schneider, A. M.; Zhao, D.; Yu, L. Recent Advances in Bulk Heterojunction Polymer Solar Cells. *Chem. Rev.* **2015**, *115*, 12666–12731.

(11) Chen, C.-C.; Chang, W.-H.; Yoshimura, K.; Ohya, K.; You, J.; Gao, J.; Hong, Z.; Yang, Y. An Efficient Triple-Junction Polymer Solar Cell Having a Power Conversion Efficiency Exceeding 11%. *Adv. Mater.* **2014**, *26*, 5670–5677.

(12) Zhang, K.; Gao, K.; Xia, R.; Wu, Z.; Sun, C.; Cao, J.; Qian, L.; Li, W.; Liu, S.; Huang, F.; Peng, X.; Ding, L.; Yip, H.-L.; Cao, Y. High-Performance Polymer Tandem Solar Cells Employing a New n-Type Conjugated Polymer as an Interconnecting Layer. *Adv. Mater.* **2016**, *28*, 4817–4823.

(13) He, Z.; Wu, H.; Cao, Y. Recent Advances in Polymer Solar Cells: Realization of High Device Performance by Incorporating Water/Alcohol-Soluble Conjugated Polymers as Electrode Buffer Layer. *Adv. Mater.* **2014**, *26*, 1006–1024.

(14) Zhao, W.; Li, S.; Yao, H.; Zhang, S.; Zhang, Y.; Yang, B.; Hou, J. Molecular Optimization Enables over 13% Efficiency in Organic Solar Cells. *J. Am. Chem. Soc.* **2017**, *139*, 7148–7151.

(15) Cheng, P.; Zhang, M.; Lau, T.-K.; Wu, Y.; Jia, B.; Wang, J.; Yan, C.; Qin, M.; Lu, X.; Zhan, X. Realizing Small Energy Loss of 0.55 eV, High Open-Circuit Voltage > 1 V and High Efficiency > 10% in Fullerene-Free Polymer Solar Cells via Energy Driver. *Adv. Mater.* **2017**, *29*, 1605216.

(16) Dai, S.; Zhao, F.; Zhang, Q.; Lau, T.-K.; Li, T.; Liu, K.; Ling, Q.; Wang, C.; Lu, X.; You, W.; Zhan, X. Fused Nonacyclic Electron Acceptors for Efficient Polymer Solar Cells. *J. Am. Chem. Soc.* **2017**, *139*, 1336–1343.

(17) Cui, Y.; Yao, H.; Gao, B.; Qin, Y.; Zhang, S.; Yang, B.; He, C.; Xu, B.; Hou, J. Fine-Tuned Photoactive and Interconnection Layers for Achieving over 13% Efficiency in a Fullerene-Free Tandem Organic Solar Cell. *J. Am. Chem. Soc.* **2017**, *139*, 7302–7309.

(18) Xiao, S.; Zhang, Q.; You, W. Molecular Engineering of Conjugated Polymers for Solar Cells: An Updated Report. *Adv. Mater.* **2017**, *29*, 1601391.

(19) Zhou, H.; Yang, L.; You, W. Rational Design of High Performance Conjugated Polymers for Organic Solar Cells. *Macromolecules* **2012**, *45*, 607–632.

(20) Liang, Y.; Yu, L. A New Class of Semiconducting Polymers for Bulk Heterojunction Solar Cells with Exceptionally High Performance. *Acc. Chem. Res.* **2010**, *43*, 1227–1236.

(21) Yao, H.; Ye, L.; Zhang, H.; Li, S.; Zhang, S.; Hou, J. Molecular Design of Benzodithiophene-Based Organic Photovoltaic Materials. *Chem. Rev.* **2016**, *116*, 7397–7457.

(22) Ye, L.; Zhang, S.; Huo, L.; Zhang, M.; Hou, J. Molecular Design toward Highly Efficient Photovoltaic Polymers Based on Two-Dimensional Conjugated Benzodithiophene. *Acc. Chem. Res.* **2014**, *47*, 1595–1603.

(23) Lu, L.; Yu, L. Understanding Low Bandgap Polymer PTB7 and Optimizing Polymer Solar Cells Based on It. *Adv. Mater.* **2014**, *26*, 4413–4430.

(24) Zheng, T.; Cai, Z.; Ho-Wu, R.; Yau, S. H.; Shaparov, V.; Goodson, T.; Yu, L. Synthesis of Ladder-Type Thienoacenes and Their Electronic and Optical Properties. *J. Am. Chem. Soc.* **2016**, *138*, 868–875.

(25) Son, H. J.; Lu, L.; Chen, W.; Xu, T.; Zheng, T.; Carsten, B.; Strzalka, J.; Darling, S. B.; Chen, L. X.; Yu, L. Synthesis and Photovoltaic Effect in Dithieno[2,3-d:2′,3′-d′]Benzo[1,2-b:4,5-b′]-dithiophene-Based Conjugated Polymers. *Adv. Mater.* **2013**, *25*, 838–843.

(26) Wu, J.-S.; Cheng, S.-W.; Cheng, Y.-J.; Hsu, C.-S. Donor-Acceptor Conjugated Polymers Based on Multifused Ladder-Type Arenes for Organic Solar Cells. *Chem. Soc. Rev.* **2015**, *44*, 1113–1154.

(27) Knall, A.-C.; Ashraf, R. S.; Nikolka, M.; Nielsen, C. B.; Purushothaman, B.; Sadhanala, A.; Hurhangee, M.; Broch, K.; Harkin, D. J.; Novák, J.; Neophytou, M.; Hayoz, P.; Sirringhaus, H.; McCulloch, I. Naphthacenodithiophene Based Polymers—New Members of the Acenodithiophene Family Exhibiting High Mobility and Power Conversion Efficiency. *Adv. Funct. Mater.* **2016**, *26*, 6961–6969.

(28) Chang, C.-Y.; Cheng, Y.-J.; Hung, S.-H.; Wu, J.-S.; Kao, W.-S.; Lee, C.-H.; Hsu, C.-S. Combination of Molecular, Morphological, and Interfacial Engineering to Achieve Highly Efficient and Stable Plastic Solar Cells. *Adv. Mater.* **2012**, *24*, 549–553.

(29) McCulloch, I.; Ashraf, R. S.; Biniek, L.; Bronstein, H.; Combe, C.; Donaghey, J. E.; James, D. I.; Nielsen, C. B.; Schroeder, B. C.; Zhang, W. Design of Semiconducting Indacenodithiophene Polymers for High Performance Transistors and Solar Cells. *Acc. Chem. Res.* **2012**, *45*, 714–722.

(30) Mai, J.; Lau, T.-K.; Li, J.; Peng, S.-H.; Hsu, C.-S.; Jeng, U. S.; Zeng, J.; Zhao, N.; Xiao, X.; Lu, X. Understanding Morphology Compatibility for High-Performance Ternary Organic Solar Cells. *Chem. Mater.* **2016**, *28*, 6186–6195.

(31) Mai, J.; Lu, H.; Lau, T.-K.; Peng, S.-H.; Hsu, C.-S.; Hua, W.; Zhao, N.; Xiao, X.; Lu, X. High Efficiency Ternary Organic Solar Cell with Morphology-Compatible Polymers. *J. Mater. Chem. A* **2017**, *5*, 11739–11745.

(32) Liao, H.-C.; Tsao, C.-S.; Lin, T.-H.; Chuang, C.-M.; Chen, C.-Y.; Jeng, U. S.; Su, C.-H.; Chen, Y.-F.; Su, W.-F. Quantitative Nanoorganized Structural Evolution for a High Efficiency Bulk Heterojunction Polymer Solar Cell. *J. Am. Chem. Soc.* **2011**, *133*, 13064–13073.

(33) Liao, H.-C.; Tsao, C.-S.; Shao, Y.-T.; Chang, S.-Y.; Huang, Y.-C.; Chuang, C.-M.; Lin, T.-H.; Chen, C.-Y.; Su, C.-J.; Jeng, U. S.; Chen, Y.-F.; Su, W.-F. Bi-hierarchical Nanostructures of Donor-Acceptor Copolymer and Fullerene for High Efficient Bulk Heterojunction Solar Cells. *Energy Environ. Sci.* **2013**, *6*, 1938–1948.

(34) Cowan, S. R.; Roy, A.; Heeger, A. J. Recombination in Polymer-Fullerene Bulk Heterojunction Solar Cells. *Phys. Rev. B: Condens. Matter Mater. Phys.* **2010**, *82*, 245207.

(35) Kyaw, A. K. K.; Wang, D. H.; Gupta, V.; Leong, W. L.; Ke, L.; Bazan, G. C.; Heeger, A. J. Intensity Dependence of Current−Voltage Characteristics and Recombination in High-Efficiency Solution-Processed Small-Molecule Solar Cells. *ACS Nano* **2013**, *7*, 4569−4577.

(36) Proctor, C. M.; Kuik, M.; Nguyen, T.-Q. Charge Carrier Recombination in Organic Solar Cells. *Prog. Polym. Sci.* **2013**, *38*, 1941−1960.

(37) Kyaw, A. K. K.; Wang, D. H.; Wynands, D.; Zhang, J.; Nguyen, T.-Q.; Bazan, G. C.; Heeger, A. J. Improved Light Harvesting and Improved Efficiency by Insertion of an Optical Spacer (ZnO) in Solution-Processed Small-Molecule Solar Cells. *Nano Lett.* **2013**, *13*, 3796−3801.

(38) Proctor, C. M.; Kim, C.; Neher, D.; Nguyen, T.-Q. Nongeminate Recombination and Charge Transport Limitations in Diketopyrrolopyrrole-Based Solution-Processed Small Molecule Solar Cells. *Adv. Funct. Mater.* **2013**, *23*, 3584−3594.

(39) Jiang, Y.; Yang, M.; Huang, X.; Gao, J.; Zhan, C.; Xiao, S. A Novel Donor-Acceptor Alternating Copolymer Based on Angular-Shaped Benzo[2,1-b:3,4-b]diselenophene for Bulk Heterojunction Solar Cells. *Polym. Chem.* **2015**, *6*, 1383−1392.

(40) Jiang, Y.; Xiao, S.; Xu, B.; Zhan, C.; Mai, L.; Lu, X.; You, W. Enhancement of Photovoltaic Performance by Utilizing Readily Accessible Hole Transporting Layer of Vanadium(V) Oxide Hydrate in a Polymer−Fullerene Blend Solar Cell. *ACS Appl. Mater. Interfaces* **2016**, *8*, 11658−11666.